Evolution of Fe bearing intermetallics during DC casting and homogenisation of an Al-Mg-Si Al alloy

S. Kumar[1], P.S. Grant and K.A.Q. O'Reilly

Department of Materials, University of Oxford, Oxford, OX1 3PH and the EPSRC Centre for Innovative Manufacturing in Liquid Metal Engineering.

Abstract

The evolution of iron (Fe) bearing intermetallics (Fe-IMCs) during direct chill (DC) casting and homogenisation of a grain refined 6063 aluminium-magnesium-silicon (Al-Mg-Si) alloy has been studied. The as-cast and homogenised microstructure contained Fe-IMCs at the grain boundaries and within Al grains. The primary α-Al grain size, α-Al dendritic arm spacing (DAS), IMC particle size and IMC three dimensional (3D) inter-connectivity increased from the edge to the centre of the as-cast billet, both α_c-AlFeSi and β-AlFeSi Fe-IMCs were identified, and overall α_c-AlFeSi was predominant. For the first time in industrial billets, the different Fe-rich IMCs have been characterised into types based on their 3D chemistry and morphology. Additionally the role of β-AlFeSi in nucleating Mg_2Si particles has been identified. After homogenisation, α_c-AlFeSi predominated across the entire billet cross-section, with marked changes in the 3D morphology and strong reductions in inter-connectivity, both supporting a recovery in alloy ductility.

Keyword: 6063 Al alloy; DC casting; Fe bearing intermetallics; Homogenisation; Intermetallic extraction;

1. Introduction

[1] Corresponding author: kumar.sundaram@materials.ox.ac.uk

Due to their high strength and good formability, AA6xxx Al alloys have found widespread applications as structural materials in the transport and building industries [1]. The alloys are direct chill (DC) cast in billet form suitable for subsequent extrusion. Due to the non-equilibrium solidification conditions in DC casting, most of the solute elements (in this system, Fe, Si and Mg) segregate into the interdendritic regions and grain boundaries of the primary α-Al [2]. This solute rich liquid leads to the formation of the inter-dendritic secondary phases, such as Fe-rich intermetallic compounds (Fe-IMCs) and strengthening Mg_2Si precipitates [3, 4]. Previous studies show that α_c-AlFeSi and β-AlFeSi are the two dominant Fe-IMCs in 6063 Al alloys [5-8]. 3D analysis of these Fe-IMCs after extraction from the primary α-Al using an Al dissolution approach revealed that α_c-Al(FeMn)Si (from now referred to as α_c-AlFeSi) had a dendritic-like morphology while β-AlFeSi had a plate-like morphology [9]. Among these IMCs, it has been noted that β-AlFeSi in particular, because of its more planar geometry, reduced the ductility of Al alloy 6063 space [6]. Therefore a post-cast homogenisation heat treatment is used commercially to encourage transformation of β to α to allow: (a) more reliable downstream deformation, typically by extrusion, (b) improved mechanical properties, especially toughness and elongation to failure, and (c) improved surface finish [5, 10-16].

Despite the apparent maturity of AA6xxx alloys there is a significant on-going effort to optimise homogenisation conditions in terms of properties, while also minimising the homogenisation time. Among the factors that govern the homogenisation response, the initial cast microstructure and the alloy chemical composition play key roles. Therefore, in developing new solidification processing routes [15] or advanced solidification technologies [17-20] that seek to promote more favourable as-cast microstructures, it is important to

understand better the link between microstructural evolution in casting and the subsequent homogenisation response of the secondary phases. For example the cooling rate and solid/liquid growth velocity in DC casting significantly affect the proportions of α_c-AlFeSi and β-AlFeSi in the final microstructure [8, 10, 21, 22]. But, since the cooling rate and growth velocity vary from position to position in the billet during DC casting [2], [23], the primary Al grain size and proportion of the Fe-IMCs and Mg_2Si across the cross-section of the billet also varies, which should be accounted for in homogenisation heat treatment optimisation. In this paper, we apply an IMC phase extraction technique, along with a series of other characterisation methods, at different positions in a AA6xxx DC cast billet to track in detail changes in the Fe-rich IMC inter-connectivity, size, morphology, type and proportion during homogenisation. The spatial variation of as-cast microstructure is shown to play a significant role in homogenisation response and the various types of IMCs and their formation and transformation are described in detail.

2. Experimental details

The chemical composition of the grain refined (Al-5Ti-1B) DC cast, ~180 mm diameter Al-Mg-Si billet is given in Table 1, measured using a Spectrolab LAVFA05A spark analyser optical emission spectrometer. Consistent with industrial practice, the cast billet was homogenised at 580 ºC for ~5 hrs. The billet before and after homogenisation was sectioned horizontally across a diameter at the billet mid-height for microstructural analysis. Samples for metallography were ground with SiC papers and then polished to 0.06 µm colloidal silica finish. Samples were also anodized with Barkers reagent [7 mL HBF_4 (48 pct) and 93 mL H_2O] for 60 s at 20 V and studied by light microscopy (Zeiss Axiophot2) under polarised light and dark field imaging conditions to assess the primary Al grain size and secondary phases. The mean linear intercept method was used to measure the primary Al grain size.

Scanning electron microscopy (SEM) was conducted in a JEOL 840A, and a JEOL 5510 equipped with a secondary electron (SE) detector, a backscattered electron (BSE) detector and an energy dispersive spectrometer (EDS). Second phase particle size distributions were measured using Axio vision image analysis software on BSE images at x500 magnification and at least 1000 particles.

Intermetallic extraction apparatus (IEA) was used to extract the intermetallic particles from the as-cast and homogenised samples. IEA uses anhydrous boiling butan-1-ol (butanol) to dissolve the α-Al matrix of the alloy while keeping the intermetallic phases intact. The intermetallics were then collected on a poly-tetrafluoroethene (PTFE) filter membrane (47 mm diameter, pore size of 0.2 μm). The phases were identified in a Philips 1700 X-ray diffractometer (XRD) operating with Cu-K_α (λ = 1.54 A) radiation at 35 kV, 50 mA and 0.05^o step size. An in-house developed calibration procedure was used for determining the relative weight fractions of α_c-AlFeSi and β-AlFeSi from XRD data, more details of which can be found in references [8, 22, 24]. The extracted particles were further analysed using a high resolution field emission gun (FEG) SEM (JEOL 840F). The approach used to measure the IMCs inter-connectivity, length of petals and length of longest facet side of platelets of the extracted particles was detailed in previous work [22]. MTDATA studio 5.10 software with NPL aluminium database V6.1 was used to predict phases as a function of temperature under various assumptions (see later).

3. Results

3.1 Primary α-Al grain analysis

The polarised light microscopy images in Fig 1(a) show the dendritic equaixed morphology of α-Al grains across the cast billet cross-section. The grain size and dendrite arm spacing (DAS) increased from the near surface to the centre of the cast billet (Fig. 1(c)). This suggests change in cooling rate along the billet cross-section. The cooling rate can be calculated from [25]

$$V = 3.57 \times 10^4 DAS^{-2.56}$$

where V is the cooling rate, Ks^{-1}. Using the observed DAS (μm), the cooling rate at distance of 15 mm, 30 mm, 60 mm and 90 mm from the billet edge towards the centre was estimated as 20.2 Ks^{-1}, 10.4 Ks^{-1}, 5.7 Ks^{-1} and 5.4 Ks^{-1} respectively, which showed good agreement with measured data [23, 26, 27]. In general during DC casting, the liquid metal is delivered from the furnace to the water cooled ring mould by a launder [23]. Once the melt comes in to contact with the mould it starts to solidify and forms a thin solid shell around the hot liquid. Further withdrawal of the base of the mould results in water directly coming into contact with the solidifying shell, and induces cooling rates of 20 K/s (near surface) to 1 K/s (billet centre) [23], similar those estimated here in this study. Because of the inevitably higher cooling rate at the billet surface, finer α-Al grains and a smaller DAS resulted in this region, as shown in Fig. 1.

After homogenisation, the α-Al grain morphology showed similar features to the as-cast structure (Figs. 1(a) and 1(b)), but the DAS became difficult to quantify due to a reduction in inter-dendritic contrast. However the grain size in the homogenised billet followed a similar trend with respect to the as-cast billet. All error bars in this manuscript indicates the standard deviation of the mean, unless stated.

3.2 Secondary phase analysis

(A) XRD analysis of extracted particles

In order to evaluate the type and proportion of the secondary phases in these relatively dilute Al alloy systems, where secondary phases fractions are less than 3 wt.%, it is most effective to extract the particles from the α-Al matrix for various types of subsequent analysis. The XRD trace from the extracted particles in Fig. 2 shows cubic α_c-AlFeSi (α_c-Al(FeMn)Si), monoclinic β-AlFeSi and cubic Mg_2Si phases along the billet cross-section, taken at distances of 15, 30, 60 and 90 mm from the billet edge towards the centre. Of the Fe-IMCs, α_c-AlFeSi showed the highest intensity peaks (> 50%) in both as-cast (Fig. 2(a)) and homogenised (Fig. 2(b)) billets. Using calibrated standards [28] to gain phase fractions, Fig. 3 shows that in the as-cast billet, the proportion of α_c-AlFeSi relative to β-AlFeSi was almost uniform across the radius. However after homogenisation heat treatment, in all locations, the homogenised billet had a higher fraction (> 90%) of α_c-AlFeSi (i.e. less β-AlFeSi). The Mg_2Si fraction was also lower in the homogenised billet. It is important to note that the pore size of the filter paper used to collect the extracted particles was 200 nm and only individual particles or cluster of particles bigger than the pore size will be present in the analysis.

(B) Metallography

The homogenised billet showed secondary phase particles at the grain boundaries (A) and within Al grains (S) (Fig. 4(a)). The particles (brighter in Fig. 4(b)) at the grain boundaries had a higher aspect ratio then particles within the grains. The larger aspect ratio Fe-IMCs particles mostly had script-like (Fig. 5(a)) and needle-like (Fig. 5(b)) morphologies, and the smaller aspect ratio particles had a rosette-like (Fig. 5(c)) morphology. Morphologies were similar in the as-cast billet [9, 22] and it was concluded that the script-like and needle-like Fe-IMC morphologies could be attributed to α_c-AlFeSi and β-AlFeSi respectively [28, 29]. The rosette-like 2D morphology was also attributed to α_c-AlFeSi [28]. However Fe-IMC

particles in the homogenised billet were smaller in size with a narrower size distribution when compared to the as-cast samples (Fig. 6), and the equivalent particle size (the diameter of a circle with the same area as the projection area of the irregular shaped particle) increased towards the centre in both the as-cast (Fig. 6(a)) and homogenised billets (Fig. 6(b)). The more spherical, minor fractions of particles within grains changed little after homogenisation, and data from these particles is not included in these plots.

Grain boundary Mg_2Si in the as-cast billet tended to be co-located with the needle-like Fe-IMCs (Fig. 7(a)), whereas Mg_2Si within α-Al grains was mostly co-located with the rosette-like Fe-IMCs (Fig. 7(b)). For example, the EDS line scan across the rosette-like region in Fig. 7(c) showed Mg_2Si and Fe-IMCs together. There was also individual needle-like Mg_2Si at the grain boundaries of the cast billet. However the Mg_2Si in the homogenised billet was coarser with an average equivalent particle size of Mg_2Si at the centre of the as-cast and homogenised billets of 1.6 ± 0.1 μm and 2.9 ± 0.2 μm, respectively. In the homogenised billet, the Mg_2Si mostly had rod-like and spherical-like morphologies at the grain boundaries.

(C) SEM analysis of extracted particles

In order to understand better the nature (inter-connectivity and morphology) of the secondary phase particles that form during the solidification and homogenisation of the DC billets, extracted particles were investigated. Critically this approach revealed that the grain boundary IMC particles in the as-cast billet were a network of highly inter-connected Fe-IMCs in 3D (Fig. 8(a)), and the inter-connectivity (Fig. 8(c)) increased towards the billet centre. High magnification imaging revealed that the as-cast Fe-IMCs were mostly dendritic/petal-like α_c-AlFeSi (Fig. 9(a)), and platelet-like β-AlFeSi (Fig. 9(b)), consistent with previous work [9, 22]. The length of the petals increased towards the billet centre (Fig.

10(a)), but there was little difference in the longest facet length of the platelets. Similar to the dendritic/petal-like particles, the platelet-like particles showed an ability to branch and adopt complex, extended 3D geometries, as well as appearing to nucleate other platelets (Fig 9(b)). Unusually, Mg_2Si was resolved forming on the flat faces and facet-sides of the β-AlFeSi (Fig. 11).

Based on this Mg_2Si interaction with β-AlFeSi platelets, confirmed by the investigation of many such instances, the Mg_2Si/β interaction was classified into three types. Type 1 was dendrite-like (Fig. 11(a)), octahedral-like (Fig. 11(b)) and cubic-like (Fig. 11(c)) with Mg_2Si on the basal face of the β-AlFeSi; Type 2 was seaweed-like Mg_2Si on the facet-sides (Fig. 11(d)); and Type 3 was fine needle-like particles on the basal face with two different directional alignments (Fig. 11(e)).

In addition, there were discrete, spherical-like particles that were not connected with the inter-dendritic secondary phase network, which suggested that they were those secondary phases observed inside grains in the earlier 2D sections. These discrete spherical-like particles were ~ 3 μm in size (Fig. 10(a)) and were either: (i) clusters of Fe-IMCs (Fig. 12(a)), (ii) clusters of Si particles (Fig. 12(b)), (iii) cubic-like Mg_2Si, or (iv) composite agglomerates of one or more of (i) to (iii). For example, Fig. 12(c) shows a composite agglomerate of Mg_2Si and Fe-IMCs. The Mg_2Si with the rosette-like Fe-IMC in Fig. 7(b) was revealed to have a more complex octagon-like morphology when viewed after extraction, as shown in Fig. 12(b).

Interestingly, the interconnectivity reduced significantly after homogenisation in all locations (Figs. 8(b) and (c)) and the billet centre retained the longest inter-connectivity length (Fig.

8(c)). The previously inter-connected Fe-IMCs fragmented during homogenisation into discrete particles, as shown in Fig. 8(b), of the form: (i) partly degraded dendritic-like α_c-AlFeSi in Fig. 9(c); (ii) near cylindrical/disc-like α_c-AlFeSi in Fig. 9(d); or (iii) spherical-like α_c-AlFeSi in in Fig. 9(e). The dendritic/petal-like Fe-IMCs in Fig. 9(c) were similar to the as-cast particles in Fig. 9(a), but were now partly dissolved at the corners and at the thin regions of the arms (indicated with arrows). The wrinkle patterns on the surface of as-cast petal-like Fe-IMC particles in Fig. 9(a) were also now absent. The length of the partly degraded/dissolved petals (Fig. 10(b)) were similar to that in the as-cast billet (Fig. 10(a)). It was difficult to resolve any needle- or platelet-like Fe-IMC particles after homogenisation, but there was a notable increased incidence of disc-like particles, e.g. Fig. 9(d), which suggested that larger platelet-like β-AlFeSi particles transformed into fine disc-like α_c-AlFeSi, and in agreement with the XRD results in Fig. 2(b). The disc-like Fe-IMC particles were mostly connected to at least two or three other discs. The average interconnected length was ~ 20 μm (Fig.10(b)).

The apparently large proportion of needle-like Fe-IMC particles in the 2D sections of the homogenised billet in Fig. 5(b) was inconsistent with the XRD quantification of the extracted phases and SEM studies. This discrepancy was in part due to the perpendicular preferred orientation of the dendritic-like particles with respect to the sectioned plane that over emphasises their proportion, even when a systematic and monotonic change in particle size distribution is measured (Fig. 6). In other words, these 2D sections not only fail to convey the correct size and morphology of the extended IMCs, but since the particles are generally far from spherical, 2D sections can also lead to incorrect quantification of phase fractions using standard metallographic approaches.

In the homogenised billet and following extraction, the Mg_2Si particles were mostly type 1, cylinder-like in Fig. 13(a) (arrow marked) and type 2, fine needle-like in Fig. 13(b), lying predominantly in two alignments. The rosette-like Fe-IMCs in Fig. 13(c), now presented with a central hole following homogenisation, and are suggested to be originally of the type shown in Figs. 7(b,c) and Fig. 12(c) but now with the central cluster of Mg_2Si dissolved during homogenisation.

4. Discussion

4.1 Evolution of IMCs during solidification

(A) Solidification sequence and Fe-IMC phase selection

For the alloy composition used in the billets here, thermodynamic simulations of the phase fractions as a function of temperature using MTDATA software and the NPL aluminium database V6.1 were performed, which are shown in Fig. 14, under conditions of equilibrium calculation (Fig. 14 (a)) and conditions of perfect elemental mixing in the liquid, but no diffusion in the solid (so called "Scheil" conditions) (Fig. 14(b,c)). Fig. 14(a) shows that the α-Al is the first phase to form on solidification. Because in the experiments and conforming to industrial practice a TiB_2-based grain refiner was used, the primary Al manifested as equiaxed α-Al grains across the billet section, and as is well-known, the dendritic nature of the grains relates to the solute-induced instability of a planar interface during their growth. Fig. 15(a) illustrates the nucleation and growth of primary α-Al dendrites at the solidifying front of a solidifying billet during DC casting.

Due to the different diffusion rates of the solute elements (Fe, Si, Mg, Mn) in the liquid and solid Al, and their differing but generally limited solid solubility limits in Al (especially Fe and Si), solute elements tended to accumulate at the growing solid-liquid interface, and

within the shrinkage liquid fraction in inter-dendritic regions. The resulting solute-rich liquid may then undergo different variant and invariant reactions as the temperature decreases further, the nature of which depend critically on the *local* composition, cooling rate and nucleation density environment. This scenario is also shown schematically in Fig. 15(a) where a Fe-IMC eutectic front develops late in the solidification sequence. Here, "local" refers to the size of the inter-dendritic regions and the length scale of their inter-connectivity. The resulting secondary phases were clearly resolved in the anodized microstructures and extracted particles (e.g. Fig. 1 and Fig. 8).

Since DC casting provides a range of cooling rates depending on casting conditions and position in the billet, the resulting secondary phases may be thermodynamically stable i.e. predictable by phase fraction calculations with appropriate data, or metastable i.e. unpredictable by calculation, or at least only with some manipulation, as in the case for β-AlFeSi here, which is generally considered metastable although frequently observed in practice. Under the assumptions in Fig. 14(b), the formation of $Al_{13}Fe_4$, α-AlFeSi, β-AlFeSi, α-AlMnSi, Mg_2Si and Si in sequence from the liquid during solidification were predicted, and in general the following possible variant and invariant solidification reactions have been suggested for 6xxx series Al alloys [7, 30-33]:

$$L \rightarrow Al_{13}Fe_4 + \alpha\text{-Al} \quad (1)$$

$$L + Al_{13}Fe_4 \rightarrow \alpha\text{-AlFeSi} + \alpha\text{-Al} \quad (2)$$

$$L \rightarrow \alpha\text{-AlFeSi} + \alpha\text{-Al} \quad (3)$$

$$L + \alpha\text{-AlFeSi} \rightarrow \beta\text{-AlFeSi} + \alpha\text{-Al} \quad (4)$$

$$L + Al_{13}Fe_4 \rightarrow \beta\text{-AlFeSi} + \alpha\text{-Al} \quad (5)$$

$$L \rightarrow \beta\text{-AlFeSi} + \alpha\text{-Al} \quad (6)$$

$L \rightarrow Mg_2Si + \alpha\text{-Al}$ (7)

$L \rightarrow \beta\text{-AlFeSi} + Mg_2Si + Si + \alpha\text{-Al}$ (8)

$L \rightarrow Mg_2Si$ (9)

$L \rightarrow \alpha\text{-AlMnSi} + Si + \alpha\text{-Al}$ (10)

The XRD analyses (Fig. 2) and SEM analyses (Figs. 6 to 12) confirmed the presence of α_c-AlFeSi, β-AlFeSi and Mg_2Si. The largest discrepancy between modelling (Fig. 14(b)) and the possible phases described by reactions 1 to 9 was the absence of $Al_{13}Fe_4$ (equation (1)) in experiment and this may arise either because soon after formation it was rapidly transformed to α- or β-AlFeSi (for which Fig. 14 offers little support), or more likely that it was comparatively difficult to nucleate and grow $Al_{13}Fe_4$ at the required rate so that once α- or β-AlFeSi were formed, it was kinetically preferred for the residual Fe-rich liquid to be transformed as further α- or β-AlFeSi, rather than through the nucleation of a new phase [8, 33]. This agrees well with the modelling when the Scheil calculations were performed without the $Al_{13}Fe_4$ phase (Fig. 14(c)). The absence of the predicted much smaller fraction of α-AlMnSi (equation (10)) was possibly due its transformation to other phases, its low fraction, or again due to its suppression by more kinetically favourable solidification reactions. Although the SEM investigations revealed discrete Si particles (Fig. 12(b)), the absence of Si in XRD analysis was probably because the volume fraction was too low for detection. It should also be noted that by comparison with previous work in [18], the present work suggests that thermodynamic predictions of phase fractions only indicate formation of β-AlFeSi, consistent with experiment, when non-equilibrium (no solid diffusion) assumptions were used.

From the as-cast and extracted morphology and length scale of α_c-AlFeSi, it was suggested that most formed directly from the liquid via eutectic reaction (3), rather than peritectic reaction (2), because the peritectic reaction implies α_c-AlFeSi forming around $Al_{13}Fe_4$ or a composite of both, for which no XRD or SEM evidence was found. By similar consideration, β-AlFeSi is suggested to form directly from the liquid through eutectic reactions (6) and/or (8).

The selection of either α_c-AlFeSi or β-AlFeSi from the cooling inter-dendritic liquid will be governed by their relative ease of nucleation and growth [2]. For nucleation, the phase with the higher nucleation temperature (small nucleation undercooling) should be preferred initially while the phase with the higher stable growth temperature (higher growth velocity) will be preferred subsequently, if its nucleation is possible. The competition between these two criteria for each phase within the local inter-dendritic environment will determine which phase(s) will be seen in practice. However, as shown in Fig. 2 and Fig. 3 in particular, at all places in the billet at the *meso*-scale, *both* α_c-AlFeSi and β-AlFeSi form. However, at the *micro*-scale α_c-AlFeSi and β-AlFeSi did not form together within any particular interdendritic (grain boundary) region. Therefore there is a stochastic, or statistical, aspect to the nucleation of AlFeSi based IMCs, depending on the chemical and physical conditions within the final, isolated solute-rich films around evolving dendrites. Even under exactly the same cooling conditions, some films may favour α_c-AlFeSi because of the particular local chemistry, or presence of un-used grain refiners (Fig. 16), oxides or other inclusions, etc., while others will favour β-AlFeSi.

(B) Primary α-Al IMC inter-connectivity and spherical droplets

All the as-cast grain boundary secondary phases form from solute-rich grain boundary films around α-Al grains. These films have a complex 3D shape, surrounding the evolving dendrites. The secondary phases form from this film and are able to extend, branch and become highly inter-connected over large distances, many times the cell or dendrite spacing or even grain size (as shown in Fig. 15(a)). The IMC particles were comparatively finer and less inter-connected nearer to the billet surface because there was a relatively high grain/liquid surface area per unit volume (smaller microstructural scale) here. Nearer the billet centre, for a constant liquid fraction, the channel width must increase because of a decrease in grain/liquid surface area per unit volume, resulting in coarser particles and greater inter-connectivity (Fig. 8).

Spherical particles within the grains, such as the examples in Fig. 7(b) and 12, form from solute-rich liquid droplets that are formed either by pinching off and isolation of the liquid in the final stages of solidification, or are deposited by solute-rich migrating liquid films around the coarsening dendrites [34], as shown in Fig. 15(a)). Consequently, these spherical droplets were not part of the inter-connected IMC network around grains. The fine structure of these solidified droplets further suggest that these droplets may be subject to relatively large undercoolings before they are able to solidify, at temperature lower than that of to the coarser grain boundary Fe-IMCs eutectic, as illustrated in Fig. 15(a).

There were also spherical composites of Si and Fe-IMC particles, similar to those reported in entrained spherical droplet experiments [33, 35] but representing only a significant minority of the IMC particles examined. It is worth remarking that if Si and Fe, as inevitable impurities in Al alloys, could be contrived to solidify in increased fractions of these

spherical-like particles or clusters, the undermining effects of more usual, extended Fe-rich IMCs on final properties might be reduced.

(C) Mg_2Si

The presence of the type 1 (dendritic-like, octahedral-like and cubic-like) and type 2 (seaweed-like) Mg_2Si particles on the surface of β-AlFeSi suggests that they formed either by eutectic reaction (7) or directly from liquid by reaction (9), where pre-existing β-AlFeSi acts as a substrate to nucleate the Mg_2Si, potentially via an intermediate compound (occasionally a Ca-rich signal was recorded by EDX from these regions). Recent transmission electron microscopy (TEM) analysis showed common orientation relationship between β-AlFeSi and Mg_2Si in a 6xxx series Al alloy [36], which supports the role of β-AlFeSi as a nucleation substrate.

Once nucleated, further growth of Mg_2Si depends on factors similar to those already described for the growth of Fe-IMCs, except the residual solute-rich liquid will tend to have ever higher concentrations of Mg and Si, since Mg_2Si develops later in the solidification sequence. The octahedral-like (Fig. 11(b)) and cubic-like (Fig. 11(c)) Mg_2Si are similar to primary Mg_2Si in the hyper-eutectic Al-Mg_2Si alloys [37], suggesting they may form directly from solute-rich liquid by reaction (9).

The different morphologies of type 1 Mg_2Si again may arise from the local solidification conditions in the residual liquid "pockets" because of interfacial instability due to the build-up of elements rejected by the growing solid phases (in this case Al and Fe may accumulate in the liquid) and physical constraints of growth in the highly restricted film geometry, and in the "holes" inside Mg_2Si particles (Fig. 11(b,c)). Type 2 seaweed-like Mg_2Si along the edges

of β-AlFeSi suggested they formed by eutectic reaction (7), and had a similar morphology to that in an Al-Mg_2Si alloy [38].

Finally, the finest-scale (~0.6μm) Mg and Si -rich needle-like particles on the surface of β-AlFeSi are solid state precipitates of Mg_2Si that formed after solidification at the interface of pre-existing β-AlFeSi and α-Al.

4.2 Evolution of Fe-IMCs during homogenisation

The higher proportion of α_c-AlFeSi in the homogenised billet arose from the β → α_c transformation. Kuijpers *et al* [11] suggested this transformation is solute diffusion controlled, initiated by the α_c-AlFeSi nucleation on the basal face of β-AlFeSi platelets; the β-AlFeSi then dissolves and α_c-AlFeSi grows by consuming released Fe, Mn and Si. They also observed an increase in Mn content in α_c-AlFeSi particles after homogenisation due to longer diffusion times [39]. In the present study, residual β-AlFeSi attached to newly transformed α_c-AlFeSi was not observed and it is estimated that more than 90% of the β-AlFeSi transformed (under these particular homogenisation conditions) instead into discrete, fine, cylinder/disc-like α_c-AlFeSi. Further, because disc-like particles were often connected to others e.g. Fig. 9(d), more than one α_c-AlFeSi crystal may nucleate from the extended area of one β-AlFeSi platelet.

An attempt was made to investigate if transformed α_c-AlFeSi might also nucleate on pre-existing α_c-AlFeSi – since there is presumably good lattice matching and low interfacial energy between them. However, no compelling microstructural evidence could be resolved, and only partly degraded eutectic α_c-AlFeSi was evident. It is possible that β-AlFeSi

dissolves in one place and re-precipitates as α_c-AlFeSi in a different region. If such events were resolvable, *in-situ* X-ray tomography might be used to study these dynamic effects.

Fig.14 suggested that as-cast Mg_2Si formed due to non-equilibrium solute segregation to the liquid during solidification and should dissolve more readily than Fe-IMCs during re-heating and isothermal homogenisation. A previous *in-situ* hot-stage investigation [28] on a 6xxx series Al alloy showed Mg_2Si particles that were not in contact with Fe-IMCs dissolved first at a lower temperature followed by the particles that were attached to Fe-IMCs. Thus the dissolution of Mg_2Si that is attached to β-AlFeSi, which was commonly observed will induce a comparatively high local Si concentration, which can be expected to affect the kinetics of the $\beta \rightarrow \alpha$ transformation, and perhaps the transformation mechanism itself.

The relatively coarse, equiaxed Mg_2Si at grain boundaries suggests that some eutectic Mg_2Si does not dissolve but firstly tends to spheriodise to reduce the interfacial area [40, 41].

Because of the dissolution and degradation of grain boundary secondary phases, mainly Fe-IMCs, IMC inter-connectivity was also notably reduced after homogenisation (Fig. 8(c)), with inter-connectivity only maintained by those particles that retained the larger petals around primary α-Al grains, as shown in Fig. 15(b). Similarly the platelet-like inter-connected β-AlFeSi breaks into fine disc-like particles during the β-AlFeSi to α_c-AlFeSi transformation leaving finer disc-like particles around grains, as also shown in Fig. 15(b). Fe-IMCs formed from spherical droplets in side primary Al persist after homogenisation, but the as-solidified Mg_2Si or Si is dissolved.

Based on these insights, summarised schematically in the Fig. 15, it is suggested that because β transformation to α_c leads to a dramatic reduction in inter-connectivity, having a relatively high β-AlFeSi and spherical Fe-IMCs fraction in the solidified billet can be advantageous as it will result in fine, less connected α_c-AlFeSi particles after homogenisation. A high fraction of inter-connected α_c-AlFeSi in the as-cast billet is harder to break-up (more thermodynamically stable), requiring longer homogenisation temperatures and times. So long as the β to α_c AlFeSi transformation is completed, finer intermetallic particles in the billet before downstream deformation process will improve both the deformation efficiency and final property of the product [15, 18].

5. Conclusions

The as-cast and homogenised microstructure of a DC cast grain refined 6063 Al alloy was studied across the billet cross-section. The primary Al grain size, dendritic arm spacing (DAS), and secondary phase particle size increased from the billet edge to the centre of the as-cast billet. When the grain size reduced, the Fe-IMCs size interconnectivity also reduced, and *vice-versa*. Fe was present as majority α_c-AlFeSi and minority β-AlFeSi IMCs in the as-cast billet, but their relative proportions were not sensitive to position. β-AlFeSi nucleated Mg_2Si during solidification, and there were additional solidified spherical droplets of further Fe-IMCs as well as Mg_2Si, Si and composite particulates within primary α-Al grains.

The homogenised billet showed little grain/dendrite coarsening and a marked elimination of inter-dendritic secondary phases. The Fe-IMC interconnectivity was reduced everywhere, most markedly at the billet surface. Of the other as-cast particles, only spherical-like Fe-IMCs persisted within the α-Al grains after homogenisation. Overall, the results showed that while homogenisation treatments are effective, nonetheless the initial as-cast microstructure,

which is influenced by the solidification conditions, exerted a strong influence on the final homogenised microstructure, affecting the size, morphology, type, β to α transformation rate and interconnectivity of the various IMCs.

Acknowledgements

The authors acknowledge the financial support of the UK Engineering and Physical Science Research Council (EPSRC grant: Centre for Innovative Manufacturing Research on Liquid Metal Engineering, EP/H026177/1) and SAPA, UK.

References

[1] O. Reiso: *Mater. Forum, 2004, vol. 28, pp. 32-46.*

[2] C.M. Allen, K.A.Q. O'Reilly, B. Cantor and P.V. Evans: *Prog. Mater. Sci., 1998, vol. 43, pp.89-170.*

[3] H. Zhu, M.J. Couper and A.K. Dahle: *JOM, 2011, vol. 63, pp. 66-71*.

[4] L. Sweet, S.M. Zhu, S.X. Gao, J.A. Taylor and M.A. Easton: *Metall. Mat. Trans. A,2011, vol. 42, pp. 1737-1749.*

[5] S. Onurlu and A. Tekin: *J. Mater. Sci., 1994, vol. 23, pp. 1652-1655*.

[6] S. Zajac, B. B. Hutchinson, A. A. Johansson and L.Q. L.-O. Gullman: *Mater. Sci. Tech., 1994, vol. 10, pp. 323-333.*

[7] M.H. Mulazimoglu, A. Zaluska, J.E. Gruzleski and F. Paray: *Metall. Mat. Trans. A, 1996, vol. 27, pp. 929-936.*

[8] G. Sha, K.A.Q. O'Reilly, B. Cantor, J. Worth and R. Hamerton: *Mater. Sci. Eng. A, 2001, Vol. 304-306, pp. 612-616.*

[9] S. Kumar, P.S. Grant and K.A.Q. O'Reilly: *Trans. Indian Inst. Met., 2012, vol. 65, pp. 553-557*.

[10] H. Tanihata, T. Sugawara, K. Matsuda and S. Ikeno: *J. Mater. Sci., 1999, vol. 34, pp. 1205-1210*.

[11] N.C.W. Kuijpers, F.J. Vermolen, K. Vuik, and S. Van Der Zwaag: *Mater. Trans., 2003, vol. 44, pp. 1448-1456*.

[12] J. Sarkar, T.R.G. Kutty, D.S. Wilkinson, J.D. Embury and D.J. Lloyd: *Mater. Sci. Eng. A, 2004, vol. 369, pp. 258-266*.

[13] Y. Birol: *J. Mater. Process. Tech., 2004, vol. 148, pp. 250-258*.

[14] K.B.S. Couto, S.R. Claves, W.H. Van Geertruyden, W.Z. Misiolek and M. Goncalves: *Mater. Sci. Tech., 2005, vol. 21, pp. 263-268*.

[15] S. Kumar, N. Hari Babu, G.M. Scamans, Z. Fan and K.A.Q. O'Reilly: *Metall. Mat. Trans. A, 2014, vol. 45, pp. 2842-2854*..

[16] J. Asensio-Lozano, B. Suárez-Peña and G.F.V. Voort: *Mater., 2014, vol. 7, pp. 4224-4242*.

[17] G.I. Eskin and I.N. Friedlyander: *Met. Sci. Heat Treat., 1962, vol. 4, pp. 154-157*.

[18] S. Kumar, N.H. Babu, G.M. Scamans and Z. Fan, *Metall. Mat. Trans. A*, 2011, vol. 42A, pp. 3141-3149.

[19] J.B. Patel, H.T. Li, M.X. Xia, S. Jones, S. Kumar, K. O'Reilly and Z. Fan: *Mater. Sci. Forum, 2014, pp. 149-154*.

[20] E. Liotti, A. Lui, R. Vincent, S. Kumar, Z. Guo, T. Connolley, I.P. Dolbnya, M. Hart, L. Arnberg, R.H. Mathiesen and P.S. Grant: *Acta. Mater., 2014, vol. 70, pp. 228-239*.

[21] C. Hsu, K.A.Q. O'Reilly, B. Cantor and P.V. Evans, *Procedings of the 4th Decennial Internation Conference on Solidification Processing, (1997)*.

[22] A. Verma, S. Kumar, P.S. Grant and K.A.Q. O'Reilly: *J. Alloys Compd., 2013, vol. 555, pp. 274-282*.

[23] D.G. Eskin, *Physical metallurgy of direct chill casting of aluminum alloys, CRC Press/Taylor & Francis, Boca Raton, 2008*.

[24] T. Smith, K. O'Reilly, S. Kumar and I. Stone: *Metall. Mat. Trans. A, 2013, vol. 44, pp. 4866-4871*.

[25] H. Westengen: *Z. Metallkd., 1982, vol. 73, pp. 360-368*.

[26] D.G. Eskin, J. Zuidema, V.I. Savran and L. Katgerman: *Mater. Sci. Eng. A, 2004, vol. 384, pp. 232-244*.

[27] Standard test procedure for aluminium alloy grain refiners, AA TP-1, the Aluminium Association, 1990.

[28] G. Sha, in: *Department of Materials, University of Oxford, Oxford, 2001*.

[29] C. Hsu, in: *Department of Materials, University of Oxford, Oxford, 1999*.

[30] G. Sha, K.A.Q. O'Reilly, B. Cantor, J.M. Titchmarsh and R.G. Hamerton: *Acta. Mater., 2003, vol. 51, pp. 1883-1897*.

[31] L.F. Mondolfo, Aluminum Alloys: Structure and Properties, (1976).

[32] L. Bäckerud, E. Król and J. Tamminen: *Solidification Characteristics of Aluminium Alloys, vol. 1, 1986*.

[33] C. Hsu, K.A.Q. O'Reilly, B. Cantor and R. Hamerton: *Mater. Sci. Eng. A, 2001, vol. 304–306, pp. 119-124*.

[34] E.D. Manson-Whitton, I.C. Stone, J.R. Jones, P.S. Grant and B. Cantor: *Acta. Mater., 2002, vol. 50, pp. 2517-2535*.

[35] C.M. Allen, K.A.Q. O'Reilly, P.V. Evans and B. Cantor: *Acta. Mater., 1999, vol. 47, pp. 4387-4403*.

[36] J.H. Li, A. Wimmer, G. Dehm and P. Schumacher: *Philos. Mag., 2014, vol. 94, pp. 830-846*.

[37] C. Li, Y.Y. Wu, H. Li and X.F. Liu: *Acta. Mater., 2011, vol. 59, pp. 1058-1067*.

[38] C. Li, Y. Wu, H. Li and X. Liu: *J. Alloys Compd., 2009, vol. 477, pp. 212-216.*

[39] N.C.W. Kuijpers, W.H. Kool, P.T.G. Koenis, K.E. Nilsen, I. Todd and S van der Zwaag: *Mater. Char., 2003, vol. 49, pp. 409-420.*

[40] M. Usta, M.E. Glicksman and R.N. Wright: *Metall. Mat. Trans. A, 2004, vol. 35, pp. 435-438.*

[41] G.V. Voort, B. Suárez-Peña and J. Asensio-Lozano: *Microsc. Microanal., 2013, vol. 19, pp. 276-284.*

Table 1 Chemical composition (in wt.%) of the AA6063 Al alloy used in this study.

Sample	Mg	Si	Fe	Mn	Cu	Ti	B	Al
AA6063	0.45	0.49	0.19	0.07	0.01	0.015	0.001	Balance

Figure Captions

Fig. 1 Polarised light microscopy images showing the α-Al grain size variation across the cross-section of the (a) as-cast and (b) homogenised billets; (c) the average grain size and DAS as a function of distance from the billet edge. The illustration inside (c) represents the position of the samples analysed, where A and B represent the near surface and centre of the billet.

Fig. 2 XRD patterns from the extracted particles formed at different positions in the (a) as-cast and (b) homogenised billets. The cross-section of the billet is illustrated in Fig. 1(c) where 15, 30, 60 and 90 mm are the distances from the billet edge towards the billet centre.

Fig. 3 Relative proportions of α_c-AlFeSi and β-AlFeSi formed at different positions in the as-cast and homogenised billets.

Fig. 4 (a) Polarised and (b) dark field light microscopy images of the microstructure in the centre region of the homogenised billet, with secondary phases at the grain boundary (A) and within the Al grains (S). Fe-IMCs and Mg_2Si are brighter in (b).

Fig. 5 BSE-SEM images of the 2D morphology of the different IMCs in the homogenised billet 90 mm from the billet edge towards the centre, indicating (a) script-like, (b) needle-like and (c) rosette-like particles.

Fig. 6 The Fe-IMC equivalent particle diameter increased from (a) 15mm from the billet edge to (b) 90mm from the billet edge for the as-cast and homogenised billets. Homogenisation resulted in smaller particles with a narrower size distribution. Measurements were made from the BSE-SEM images of the metallography samples, shown as insets.

Fig. 7 BSE-SEM images from the as-cast billet showing Mg_2Si (darker particle) associated with (a) needle-like and (b) rosette-like Fe-IMCs (brighter particle). The EDS line scan in (c) shows the composition variation along the rosette-like particle in (b).

Fig. 8 SE FEG-SEM images of the IMCs extracted at different location in the (a) as-cast and (b) homogenised billets; (c) is the measured average length of the inter-connectivity for the IMCs at different positions.

Fig. 9 SE FEG-SEM images of the extracted particles revealing (a) dendrite-like, (b) platelet-like, (c) partially dissolved dendrite-like, (d) disc-like, and (e) rosette-like

particles. Where (a-b) are from as-cast billet and (c-e) are from homogenised billet. Arrows indicate the partly dissolved regions.

Fig. 10 Length and size of IMC particles extracted at different position from the (a) as-cast and (b) homogenised billets.

Fig. 11 SE SEM images of the extracted particles showing association of Mg.Si rich particles (arrowed) with β-AlFeSi.

Fig. 12 SE FEG-SEM images showing a (a) spherical cluster of Fe-IMC particles, (b) spherical cluster of Si rich particles, and (b) composite of Mg_2Si and Fe-IMC particles, from the as-cast billet.

Fig. 13 SE SEM images of the extracted particles from the homogenised billet showing (a) rod-like Mg_2Si, (b) association of Mg-Si rich particles with partly degraded α_c-AlFeSi, and (c) rosette-like AlFeSi with a hole at the centre.

Fig. 14 Thermodynamic calculations of phase fraction in alloy 6063, assuming (a) equilibrium, and (b,c) Scheil solidification conditions. Where (c) is Scheil simulation performed without $Al_{13}Fe_4$.

Fig. 15 Schematic representation of the (a) solidification sequence in the 6063 billet during DC casting and (b) the evolution of the microstructure during the homogenisation heat treatment.

Fig. 16 SE FEG-SEM images of extracted particles from the as-cast billet with Ti-rich particles (arrowed) associated with (a) α_c-AlFeSi and (b) β-AlFeSi.

Figure 1

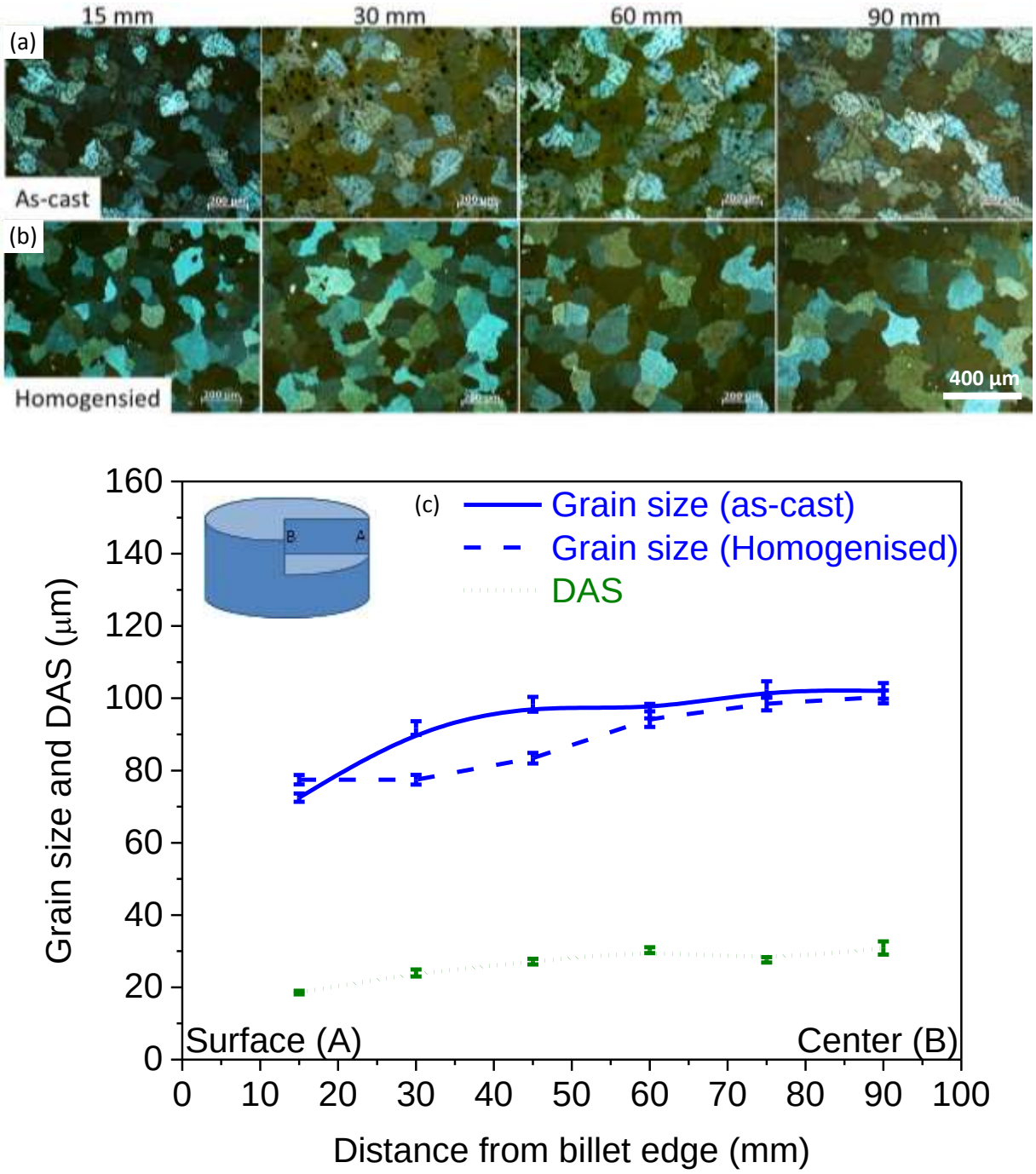

Fig. 1 Polarised light microscopy images showing the α-Al grain size variation across the cross-section of the (a) as-cast and (b) homogenised billets; (c) the average grain size and DAS as a function of distance from the billet edge. The illustration inside (c) represents the position of the samples analysed, where A and B represent the near surface and centre of the billet.

Figure 2

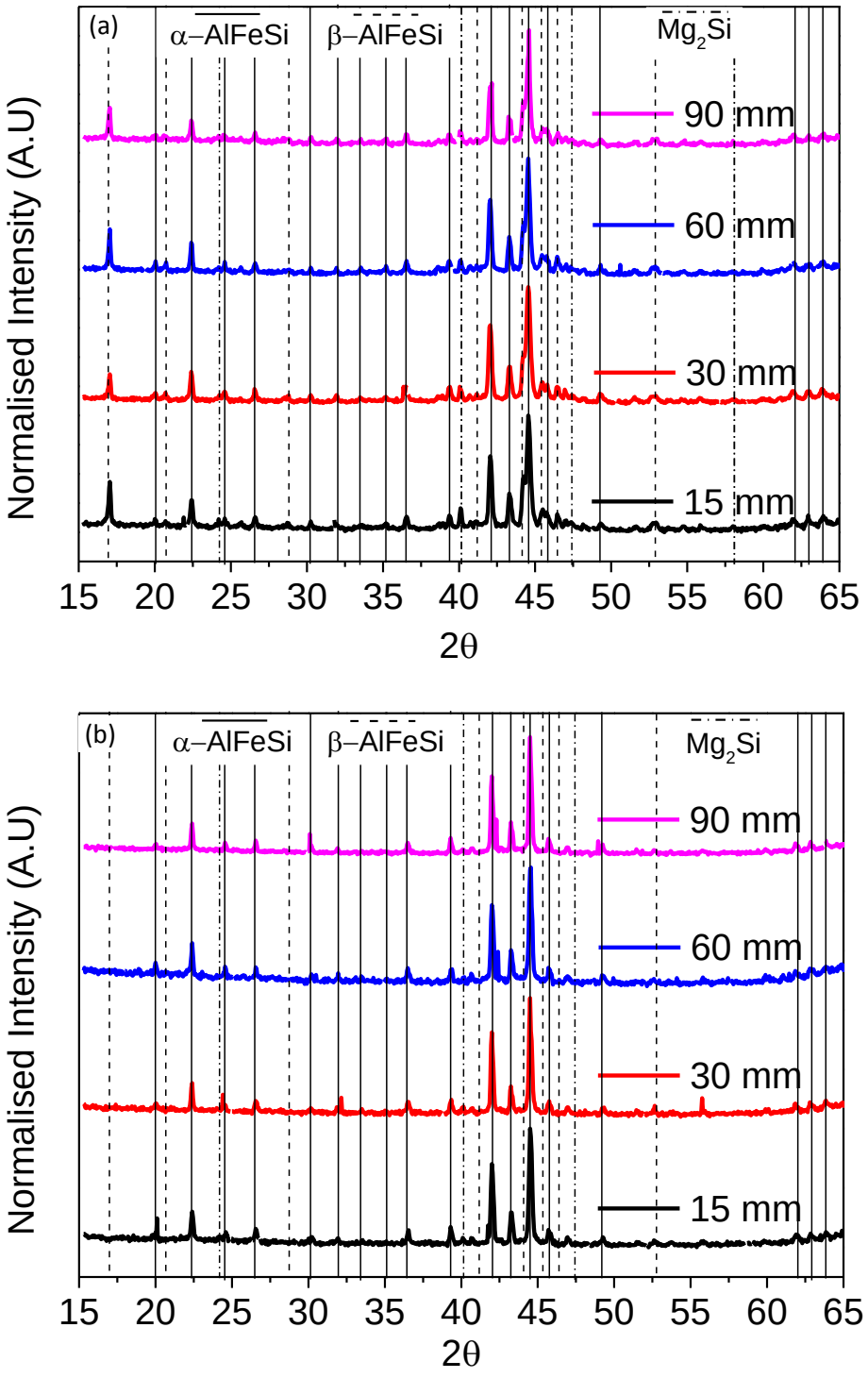

Fig. 2 XRD patterns from the extracted particles formed at different positions in the (a) as-cast and (b) homogenised billets. The cross-section of the billet is illustrated in Fig. 1(c) where 15, 30, 60 and 90 mm are the distances from the billet edge towards the billet centre.

Figure 3

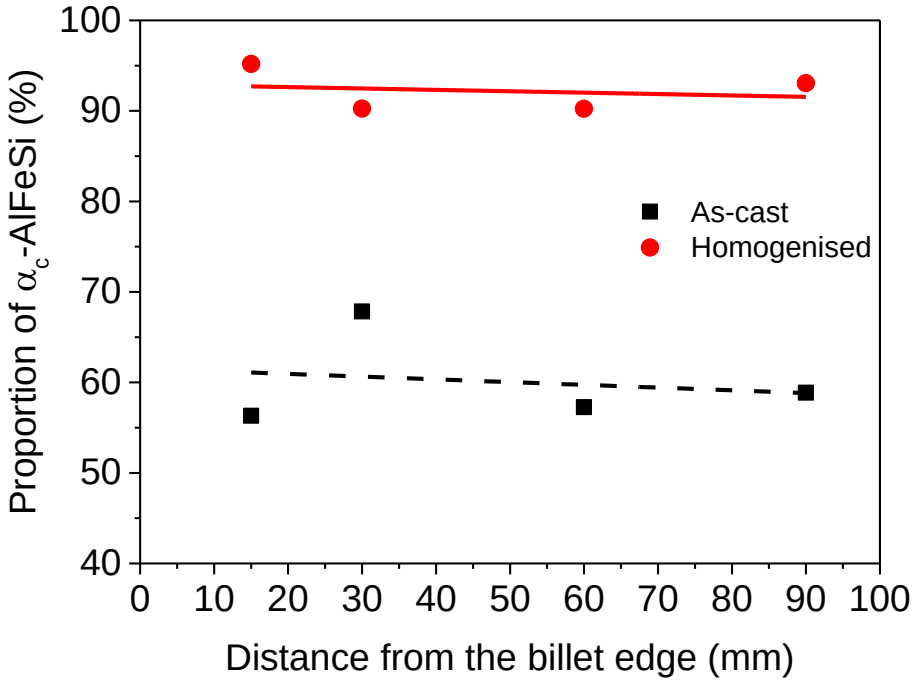

Fig. 3 Relative proportions of α_c-AlFeSi and β-AlFeSi formed at different positions in the as-cast and homogenised billets.

Figure 4

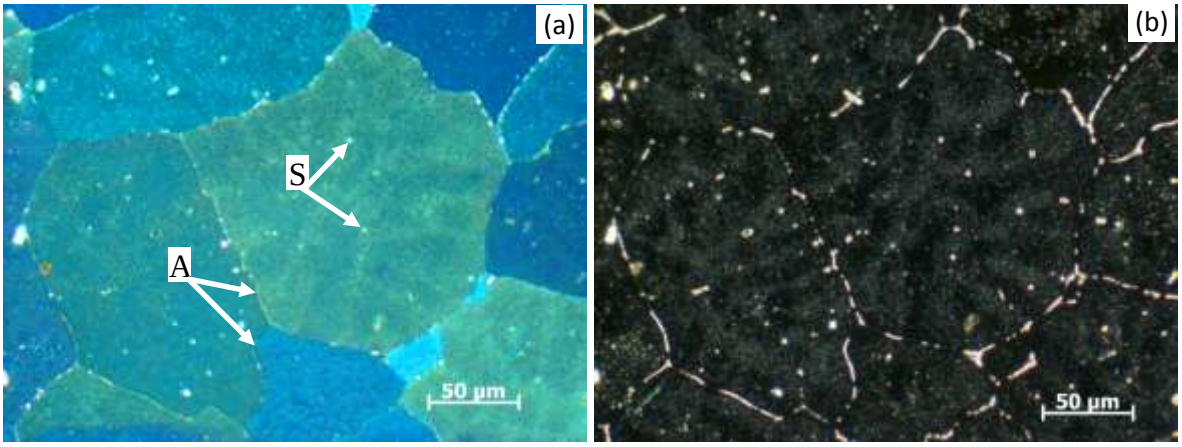

Fig. 4 (a) Polarised and (b) dark field light microscopy images of the microstructure in the centre region of the homogenised billet, with secondary phases at the grain boundary (A) and within the Al grains (S). Fe-IMCs and Mg_2Si are brighter in (b).

Figure 5

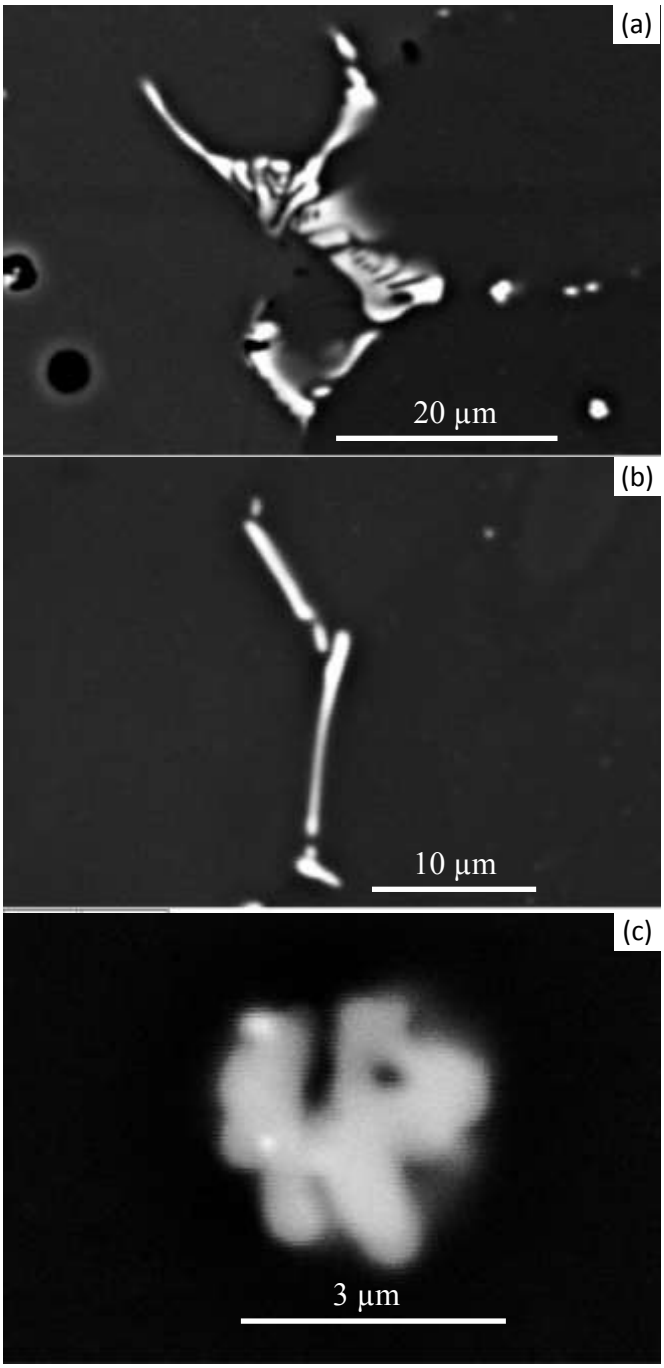

Fig. 5 BSE-SEM images of the 2D morphology of the different IMCs in the homogenised billet 90 mm from the billet edge towards the centre, indicating (a) script-like, (b) needle-like and (c) rosette-like particles.

Figure 6

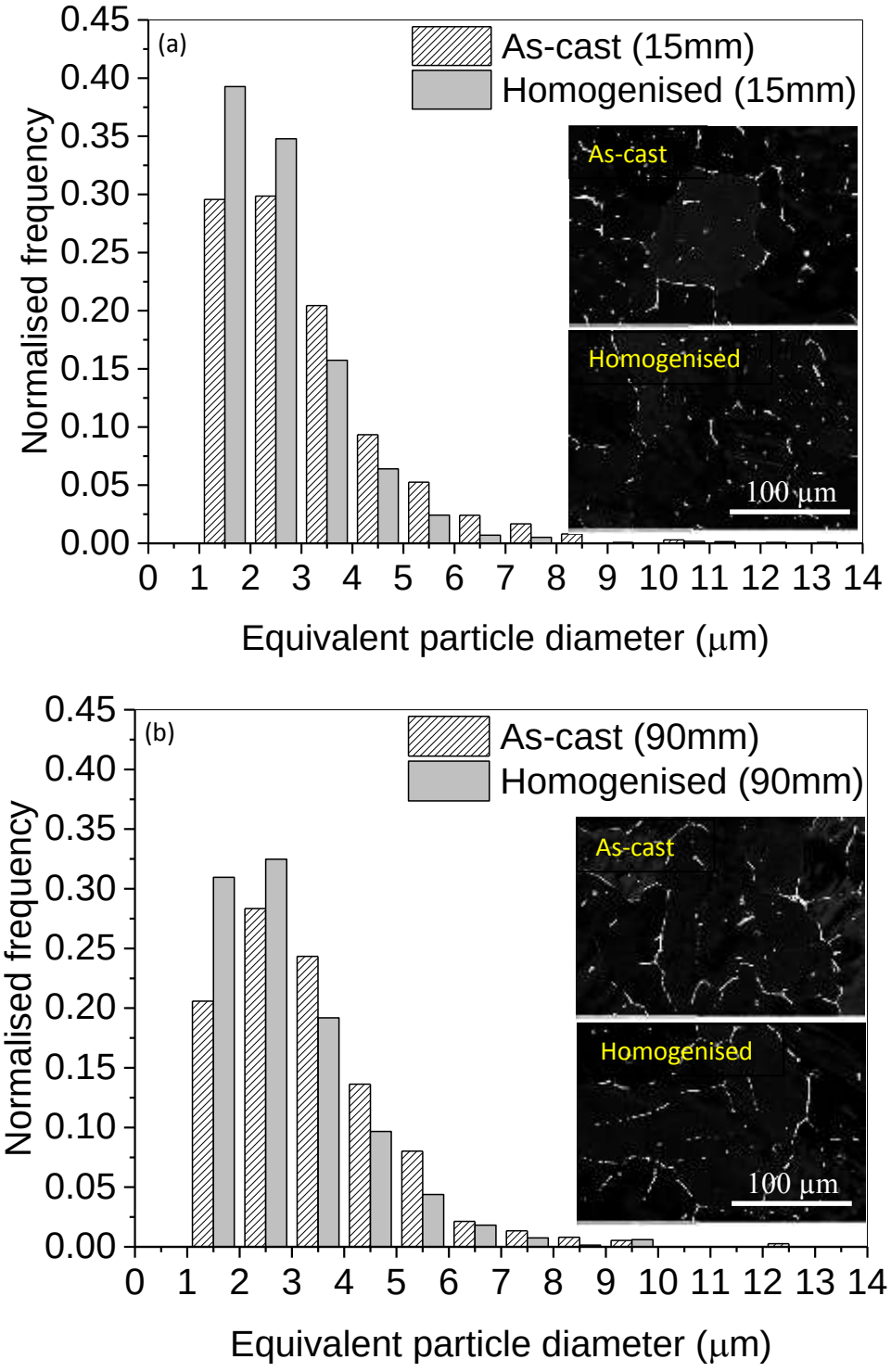

Fig. 6 The Fe-IMC equivalent particle diameter increased from (a) 15mm from the billet edge to (b) 90mm from the billet edge for the as-cast and homogenised billets. Homogenisation resulted in smaller particles with a narrower size distribution. Measurements were made from the BSE-SEM images of the metallography samples, shown as insets.

Figure 7

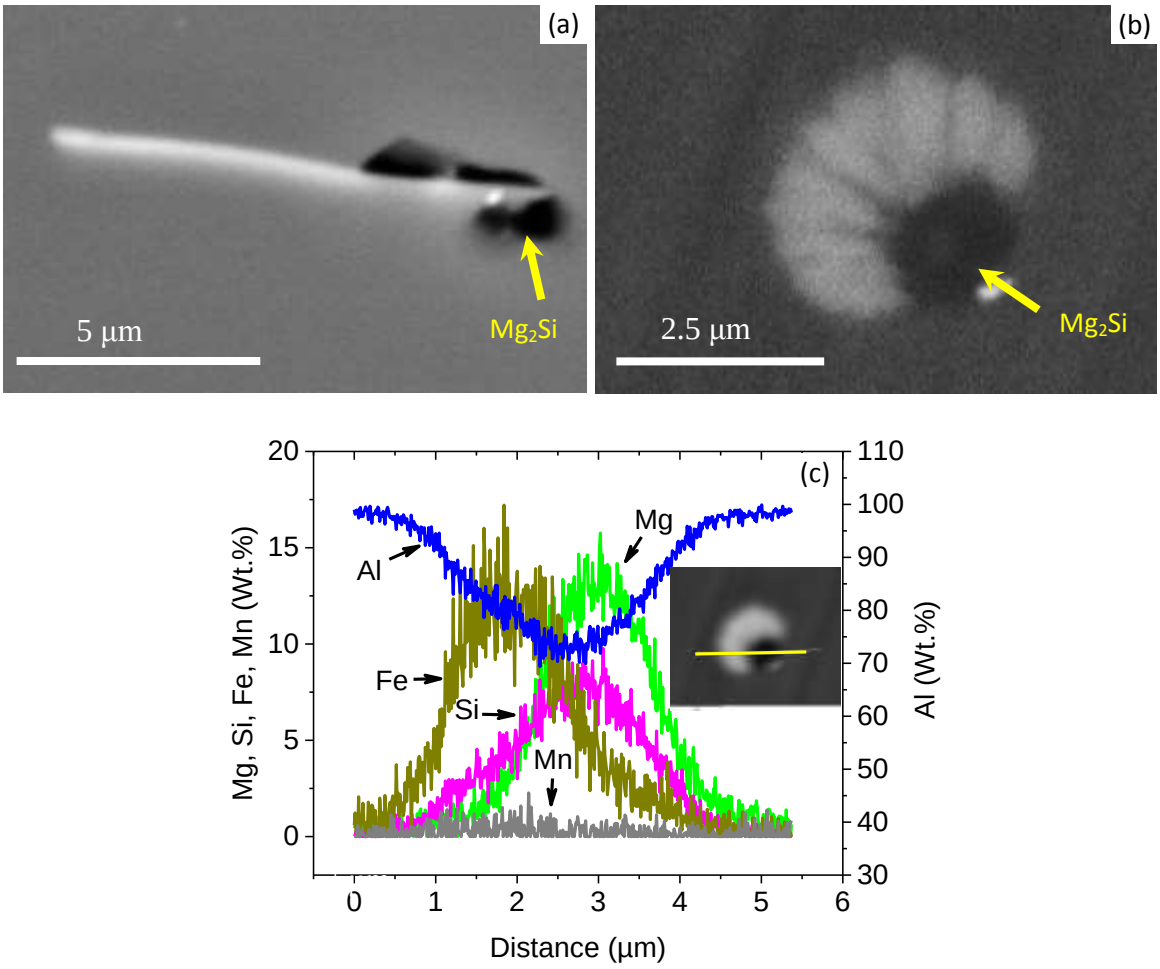

Fig. 7 BSE-SEM images from the as-cast billet showing Mg_2Si (darker particle) associated with (a) needle-like and (b) rosette-like Fe-IMCs (brighter particle). The EDS line scan in (c) shows the composition variation along the rosette-like particle in (b).

Figure 8

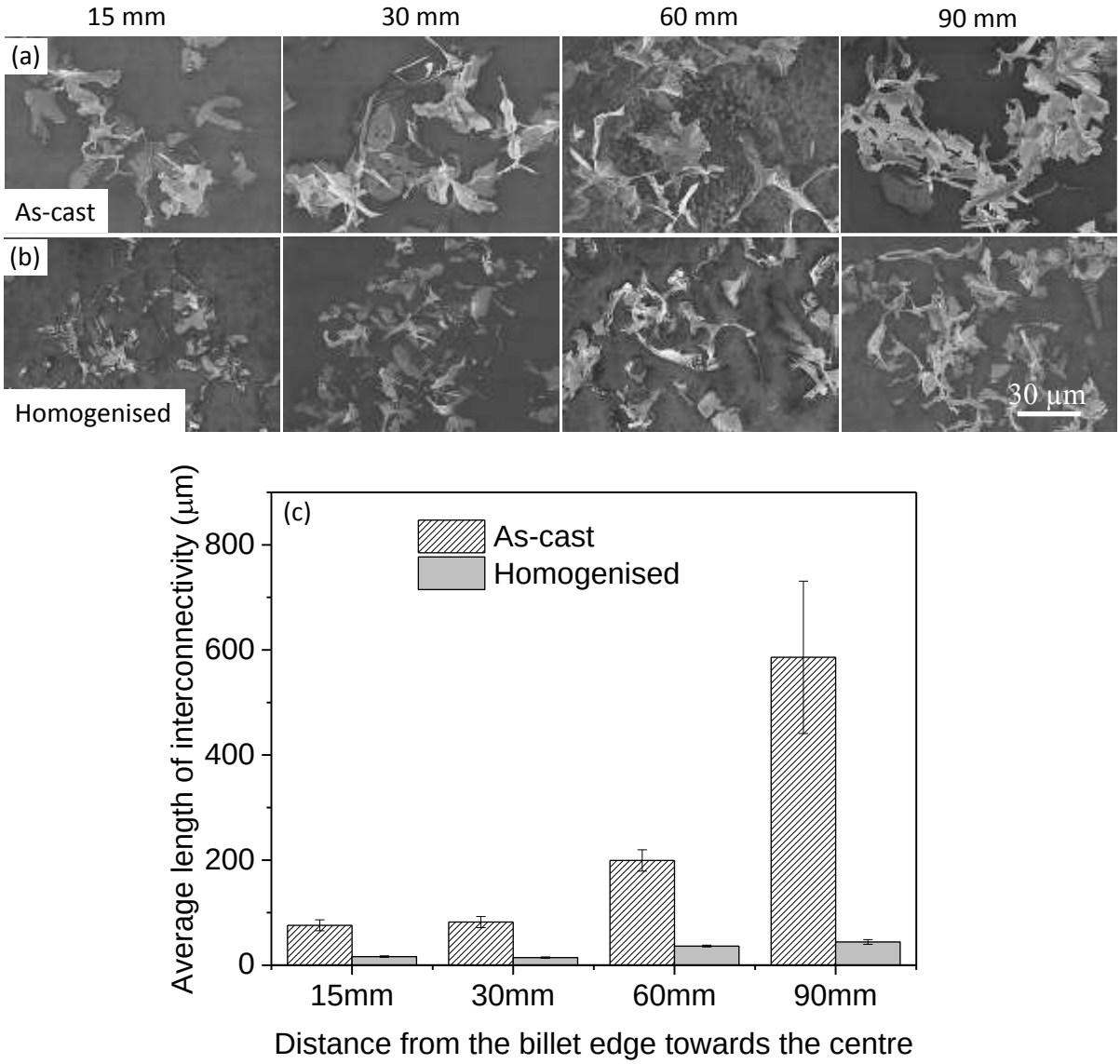

Fig. 8 SE FEG-SEM images of the IMCs extracted at different location in the (a) as-cast and (b) homogenised billets; (c) is the measured average length of the inter-connectivity for the IMCs at different positions.

Figure 9

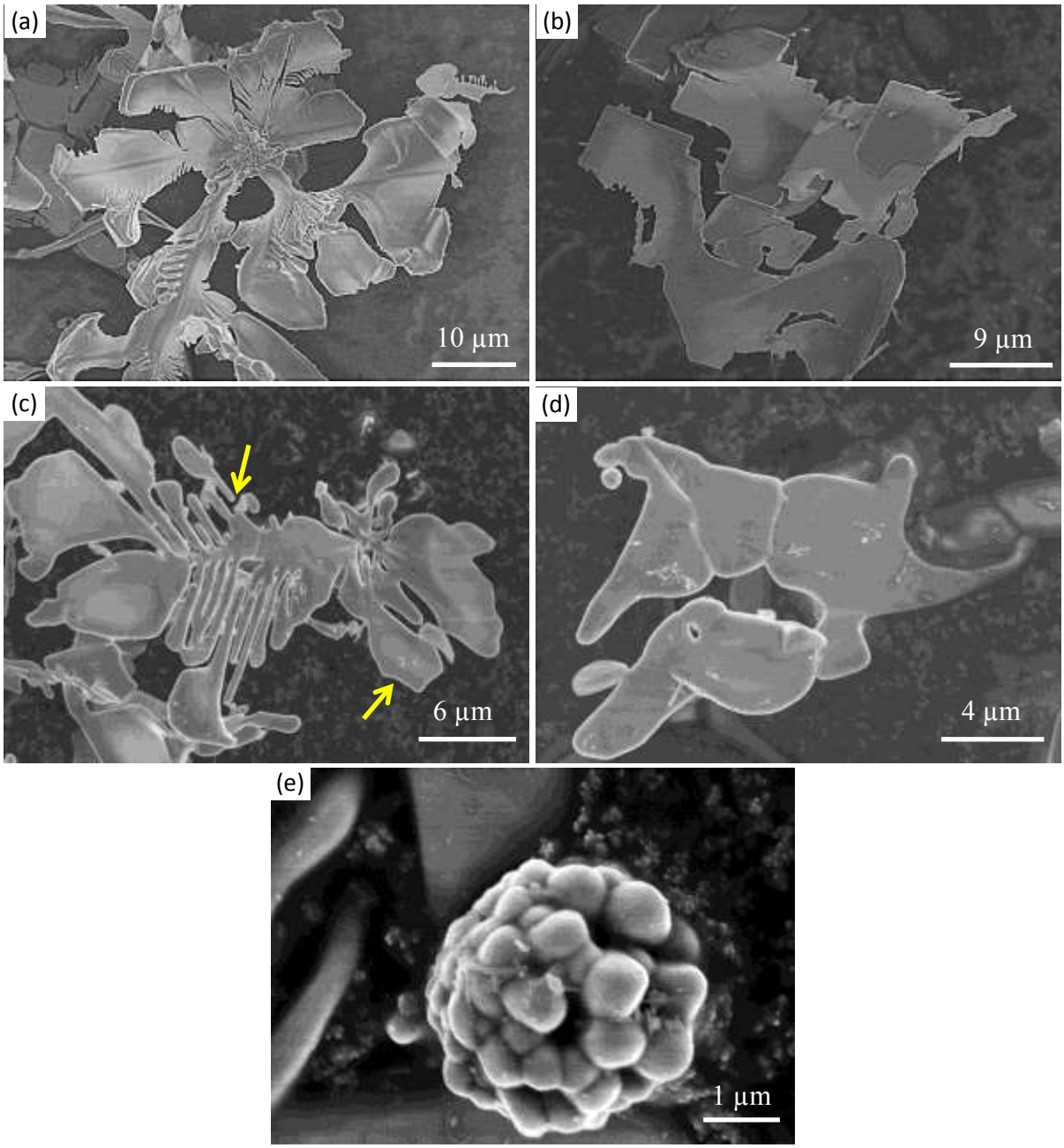

Fig. 9 SE FEG-SEM images of the extracted particles revealing (a) dendrite-like, (b) platelet-like, (c) partially dissolved dendrite-like, (d) disc-like, and (e) rosette-like particles. Where (a-b) are from as-cast billet and (c-e) are from homogenised billet. Arrows indicate the partly dissolved regions.

Figure 10

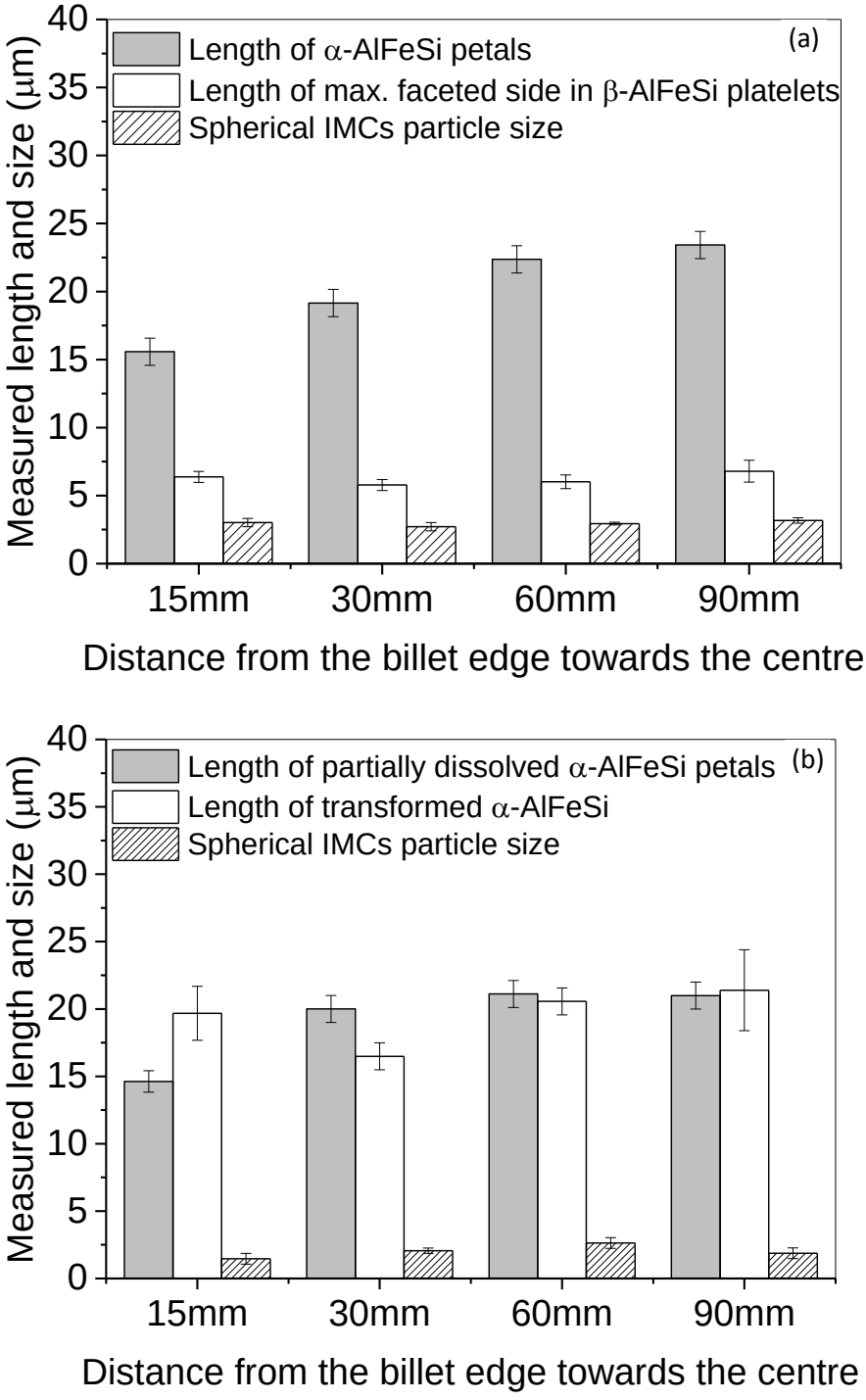

Fig. 10 Length and size of IMC particles extracted at different position from the (a) as-cast and (b) homogenised billets.

Figure 11

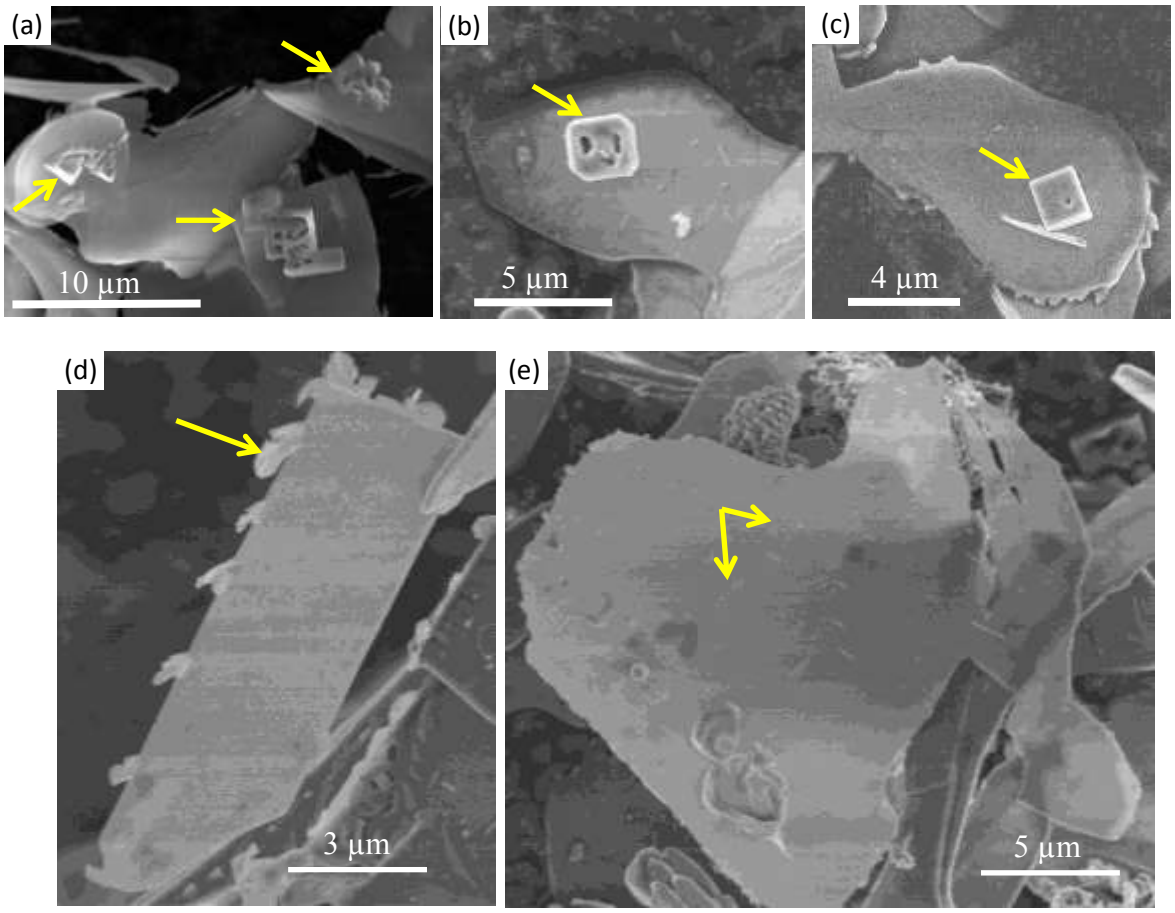

Fig. 11 SE SEM images of the extracted particles showing association of Mg.Si rich particles (arrowed) with β-AlFeSi.

Figure 12

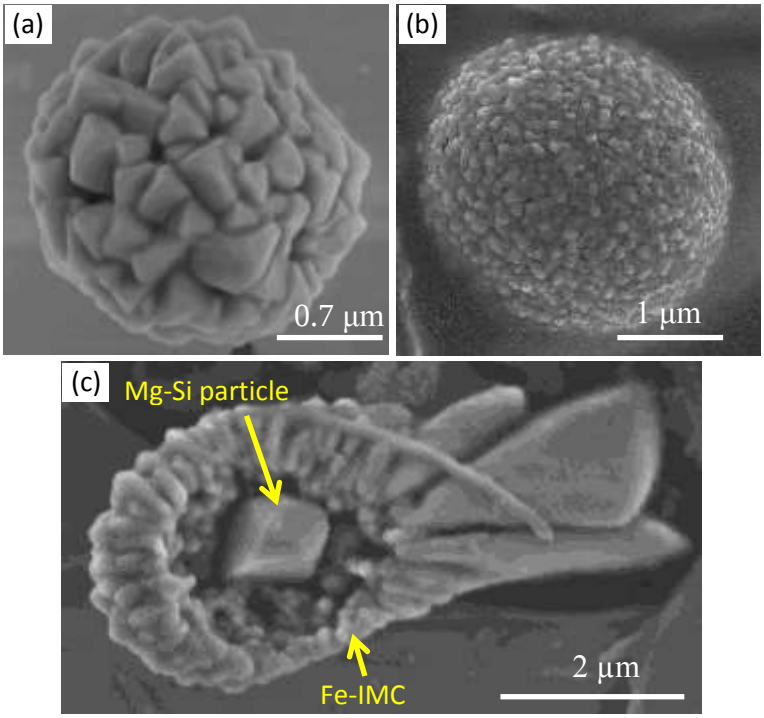

Fig. 12 SE FEG-SEM images showing a (a) spherical cluster of Fe-IMC particles, (b) spherical cluster of Si rich particles, and (b) composite of Mg_2Si and Fe-IMC particles, from the as-cast billet.

Figure 13

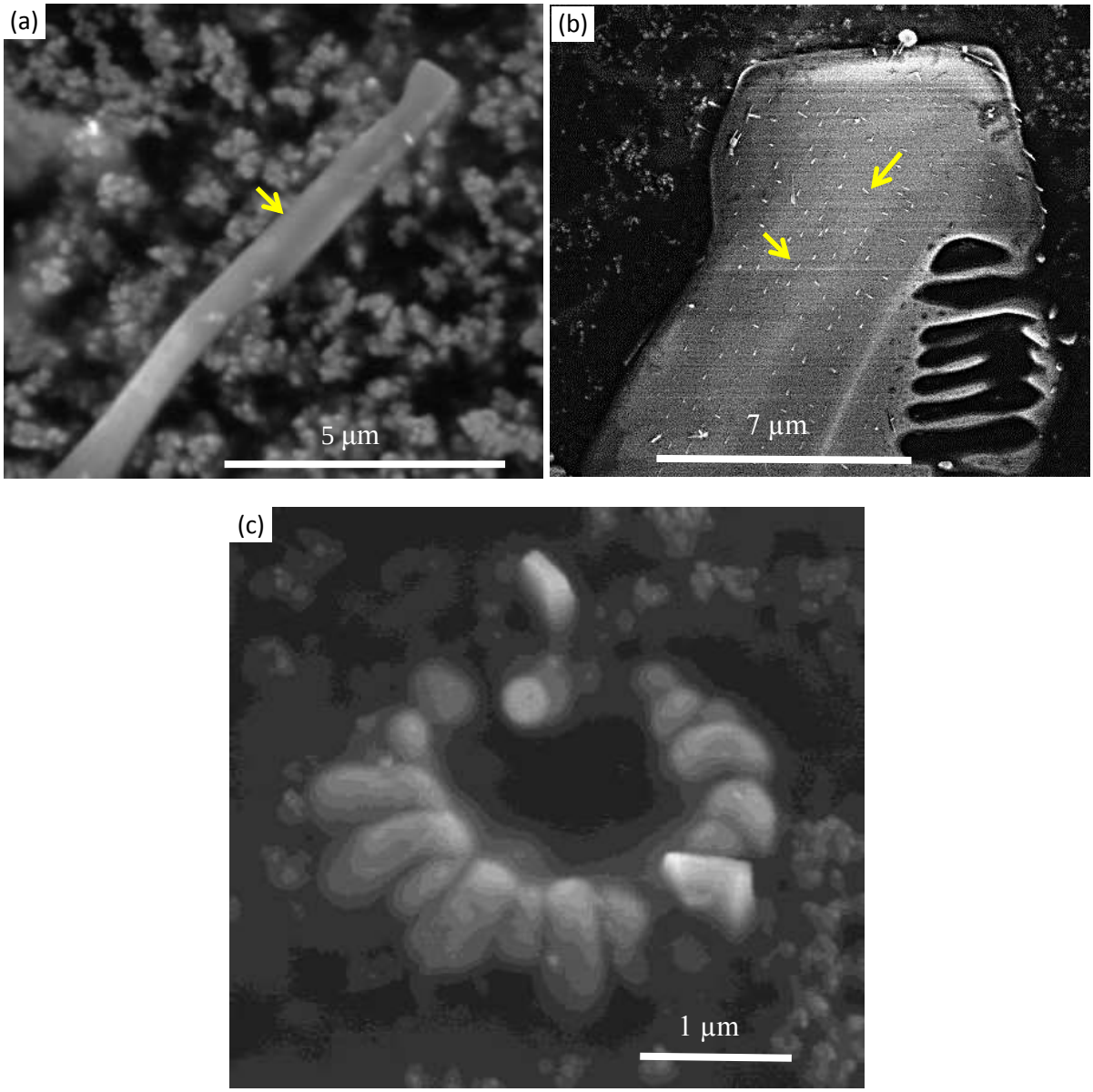

Fig. 13 SE SEM images of the extracted particles from the homogenised billet showing (a) rod-like Mg_2Si, (b) association of Mg-Si rich particles with partly degraded α_c-AlFeSi, and (c) rosette-like AlFeSi with a hole at the centre.

Figure 14

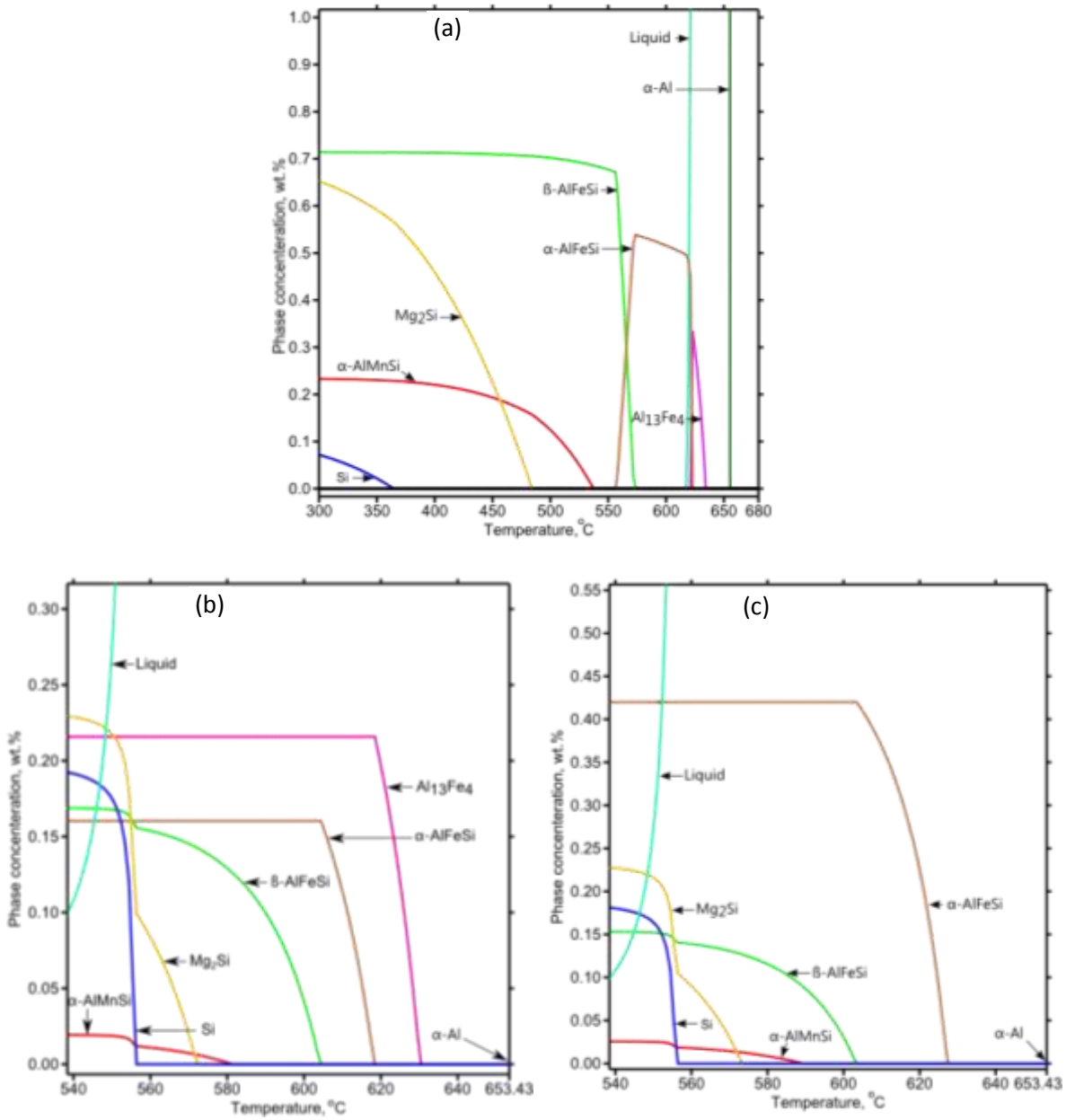

Fig. 14 Thermodynamic calculation of phase fraction in alloy 6063, assuming (a) Equilibrium, and (b,c) Scheil solidification conditions. Where (c) is Scheil simulation performed without $Al_{13}Fe_4$.

Figure 15

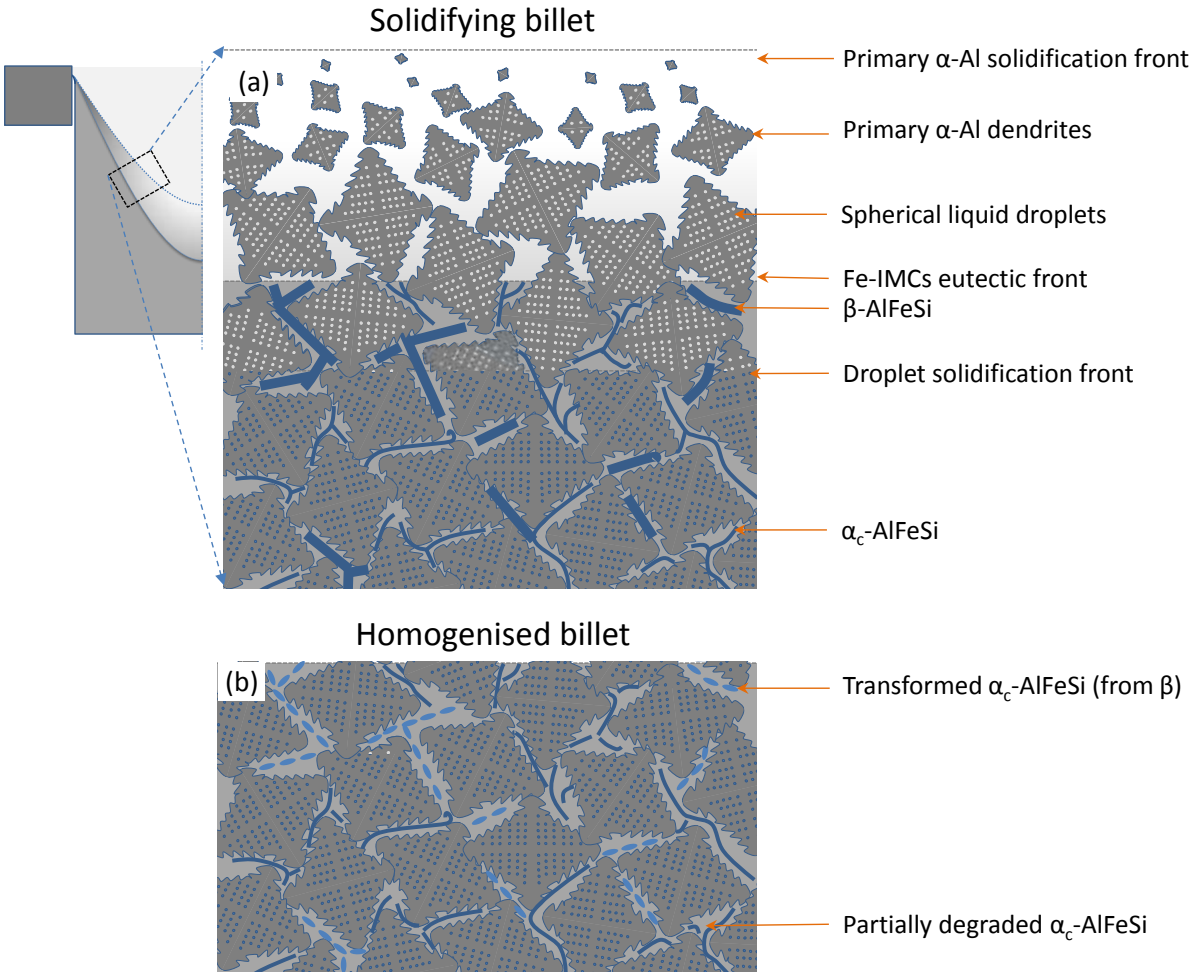

Fig. 15 Schematic representation of the (a) solidification sequence in the 6063 billet during DC casting and (b) the evolution of the microstructure during the homogenisation heat treatment.

Figure 16

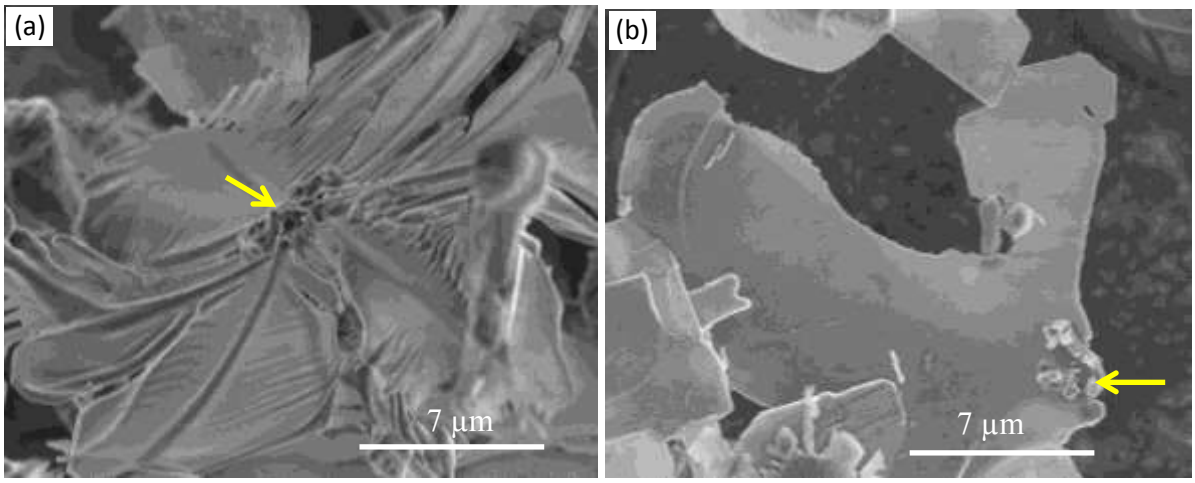

Fig. 16 SE FEG-SEM images of extracted particles from the as-cast billet with Ti-rich particles (arrowed) associated with (a) α_c-AlFeSi and (b) β-AlFeSi.